

Electronic Supplementary Information for

**Asymmetrically strained *hcp* rhodium sublattice stabilized by
1D covalent boron chains as an efficient electrocatalyst**

Zhenyu Li,^{a,b,#} Xuan Ai,^{a,#} Hui Chen,^{a,#} Xiao Liang,^a Xiaotian Li,^b Dong
Wang,^c Xiaoxin Zou^{a,*}

^a*State Key Laboratory of Inorganic Synthesis and Preparative Chemistry, College of
Chemistry, Jilin University, Changchun 130012, P. R. China.*

^b*College of Materials Science and Engineering, Jilin University, Changchun 130022,
P. R. China.*

^c*College of Chemical Engineering, Sichuan University, Chengdu 610065, P. R. China.*

‡ *Z. Li, X. Ai and H. Chen contributed equally to this work.*

* E-mail: xxzou@jlu.edu.cn

1 Experimental Section

1.1 Chemicals and Reagents.

Potassium hexachlororhodate (K_3RhCl_6), potassium fluoroborate (KBF_4) and platinum tetrachloride ($PtCl_4$, 99.9%) were obtained from Aladdin Chemistry Co., Ltd. Magnesium boride (MgB_2) was purchased from Alfa Aesar Chemicals Co., Ltd. Ethanol, isopropanol and sulfuric acid (H_2SO_4) were purchased from Beijing Chemical Factory. Magnesite powder (Mg) was obtained from Xilong Chemical Reagent Co., Ltd. Platinum on graphitized carbon (20 wt% Pt/C) and Nafion perfluorinated resin solution were bought from Sigma-Aldrich. Highly purified water ($>18\text{ M}\Omega\text{ cm}$ resistivity) was provided by a PALL PURELAB Plus system.

1.2 Materials Synthesis.

1.2.1 Synthesis of RhB particles. K_3RhCl_6 (108.23 mg, 0.25 mmol) and MgB_2 (17.22 mg, 0.38 mmol) were mixed in a mortar, and then the homogeneous mixture was placed into a quartz tube. The quartz tube with above mixture was sealed in a vacuum atmosphere (0.8 Pa). The RhB sample was produced by annealing the as-sealed quartz tube at $700\text{ }^\circ\text{C}$ for 4 h at a rate of $3\text{ }^\circ\text{C min}^{-1}$ in a muffle furnace. The as-synthesized product was treated in a 0.5 M H_2SO_4 solution to remove redundant MgB_2 and by-product (*i.e.*, KCl, $MgCl_2$). Finally, the resulting precipitate was washed several times with deionized water and ethanol, and dried at $80\text{ }^\circ\text{C}$ to obtain RhB.

1.2.2 Synthesis of B-Rh particles. K_3RhCl_6 (108.23 mg, 0.25 mmol) and MgB_2 (17.22 mg, 0.38 mmol) were mixed in a mortar, and then the homogeneous mixture was placed into a quartz tube. The quartz tube with above mixture was sealed in a vacuum atmosphere (0.8 Pa). The B-Rh sample was produced by annealing the as-sealed quartz tube at $500\text{ }^\circ\text{C}$ for 4 h at a rate of $3\text{ }^\circ\text{C min}^{-1}$ in a muffle furnace. The as-synthesized black powder was treated in a 0.5 M H_2SO_4 solution to remove redundant MgB_2 and by-product (*i.e.*, KCl, $MgCl_2$). Finally, the resulting precipitate was washed several times with deionized water and ethanol, and dried at $80\text{ }^\circ\text{C}$ to obtain B-Rh.

1.2.3 Synthesis of Rh nanoparticles. K_3RhCl_6 (108.23 mg, 0.25 mmol) and Mg powder (9.12 mg, 0.38 mmol) were mixed in a mortar, and then the homogeneous mixture was placed into a quartz tube. The quartz tube with above mixture was sealed in a vacuum atmosphere (0.8 Pa). The Rh sample was produced by annealing the as-sealed quartz tube at $500\text{ }^\circ\text{C}$ for 4 h at a rate of $3\text{ }^\circ\text{C min}^{-1}$ in a muffle furnace. The as-synthesized black powder was treated in a 0.5 M H_2SO_4 solution to remove redundant

MgB₂ and by-product (*i.e.*, KCl, Mg). Finally, the resulting precipitate was washed several times with deionized water and ethanol, and dried at 80 °C to obtain Rh.

1.2.4 Synthesis of Rh₇B₃ particles. K₃RhCl₆ (108.23 mg, 0.25 mmol), MgB₂ (17.22 mg, 0.38 mmol) and KBF₄ (20 mg, 0.25 mmol) were mixed in a mortar, and then the homogeneous mixture was placed into a quartz tube. The quartz tube with above mixture was sealed in a vacuum atmosphere (0.8 Pa). The Rh₇B₃ sample was produced by annealing the as-sealed quartz tube at 600 °C for 4 h at a rate of 3 °C min⁻¹ in a muffle furnace. The as-synthesized black powder was treated in a 0.5 M H₂SO₄ solution to remove redundant MgB₂ and by-product (*i.e.*, KCl, MgCl₂). Finally, the resulting precipitate (*eg.*, KBF₄) was washed several times with deionized water and ethanol, and dried at 80 °C to obtain Rh₇B₃.

1.2.5 Synthesis of Pt particles. PtCl₄ (84.2 mg, 0.25 mmol) and Mg (24.3 mg, 1 mmol) were mixed in a mortar, and then the homogeneous mixture was placed into a quartz tube. The quartz tube with above mixture was sealed in a vacuum atmosphere (0.8 Pa). The product of Pt was produced by annealing the as-sealed quartz tube at 500 °C for 4 h at a rate of 3 °C min⁻¹ in a muffle furnace. The as-synthesized black powder was treated in a 0.5 M H₂SO₄ solution to remove redundant Mg and by-product (*i.e.*, MgCl₂). Finally, the resulting precipitate was washed several times with deionized water and ethanol, and dried at 80 °C to obtain Pt.

1.3 Material Characterizations.

The powder X-ray diffraction (XRD) patterns of the materials were obtained with a Rigaku D/Max 2550 X-ray diffractometer with Cu K α radiation ($\lambda = 1.5418 \text{ \AA}$). The scanning electron microscope (SEM) images, energy dispersive X-ray (EDX) spectroscopy and EDX elemental mapping were obtained with a JEOL JSM 6700F electron microscope. The transmission electron microscope (TEM) images and high resolution TEM (HRTEM) images were recorded in a Philips-FEI Tecnai G2STwin microscope equipped with a field emission gun operating at 200 kV. X-ray photoemission spectroscopy (XPS) measurements were performed on a Thermo Fisher Scientific ESCALAB 250Xi with photoelectron spectroscopy system using a monochromatic Al K α (1486.6 eV) X-ray source.

1.4 Electrochemical Measurements.

All electrochemical tests were conducted by using a standard three-electrode system on a CHI 660E electrochemical workstation. First, 8 mg of the RhB powder,

400 μL of isopropanol and 400 μL of conductive polymer binder were ultrasonically dispersed to produce the catalyst ink. Next, 4 μL of catalyst ink was dropped onto the glassy carbon electrode (GCE) with a diameter of 3 mm. The loading mass of catalyst was 0.562 mg/cm^2 on the GCE. The GCE coated with the catalyst ink, a carbon rod, and saturated calomel electrode (SCE) electrode were served as the working electrode, counter electrode and reference electrode, respectively.

The SCE was calibrated according to the method proposed by Boettcher and co-workers.¹ Linear sweep voltammetry (LSV) measurements were conducted with the scan rate of 1 mV s^{-1} and compensated by 85% iR -drop. The potential (or overpotential) was normalized with respect to the reversible hydrogen electrode (RHE), according to Eqn. 6:

$$E_{\text{vs.RHE}} = E_{\text{vs.SCE}} + 0.263 \text{ eV} + 0.059\text{pH} \quad \text{Eqn. 1}$$

For comparative purpose, the catalytic activities of Rh, B-Rh, Pt and commercial 20 wt.% Pt/C with the same catalyst loading were evaluated under the same conditions as above.

1.4.1 Estimation of electrochemically active surface area (ECSA). The geometric double layer capacitance (C_{dl}) is employed to estimate the effective electrochemical active surface area (ECSA) of all the samples. C_{dl} was determined by taking cyclic voltammetry (CV) measurements with various scan rates (10, 20, 30, 40, 50, 60, 70, 80, 90 and 100 mV/s) in the potential windows of 0.4 - 0.5 V *versus* SCE. In order to obtain a stable CV curve and ensure consistency in the measurements, the sweep segments were set to 30. Subsequently, a linear trend was obtained by plotting the difference of current between the anodic and cathodic sweeps ($J_{\text{anodic}} - J_{\text{cathodic}}$) at 0.45 V *versus* SCE against the scan rate. The slope was calculated by fitting the above line, which then the slope is equal to twice C_{dl} . The twice of C_{dl} value is proportional to the ECSA of the catalyst. The ECSA of catalyst on GCE is estimated according to Eqn. 7:

$$\text{ECSA} = \frac{C_{\text{dl}}}{C_s} \quad \text{Eqn. 2}$$

where C_s is the specific capacitance of the sample, and the value of C_s is 0.04 mF/cm^2 in this work.

1.4.2 Determination of Faradaic efficiency. Faradaic efficiency of a catalyst is estimated by the ratio of the amount of H_2 generated in the experiment to theoretical

value. The H₂ amount during experimental process was measured by a water drainage method by our previously work report.² The theoretical amount of H₂ evolved was calculated according to the Faraday law, which states that the passage of 96485.4 C charge causes 1 equivalent of reaction.

2. Theoretical Section

The generalized gradient approximation (GGA) with the Perdew-Burke-Ernzerhof (PBE) exchange correlation functional³ and a 400 eV cutoff for the plane-wave basis set⁴ were employed to perform all the DFT computations of the materials within the frame of *Vienna ab initio simulation package* (VASP).⁵⁻⁶ For all theoretical models, the convergence threshold was set as 10⁻⁴ eV in energy and 0.02 eV Å⁻¹ in force. The Brillouin zones were sampled by Monkhorst-Pack⁷ 9 × 9 × 7 (RhB, RhC and RhN), 11 × 11 × 7 (*hcp*-Rh), 9 × 9 × 9 (Pt) and 11 × 11 × 11 (*fcc*-Rh) *k*-point grid for geometric optimization of bulk models, 5 × 5 × 1 for all slab models and 7 × 7 × 1 *k*-point grid was used to calculate the DOS of slab models. The correction of *van der Waals* interaction was included using the DFT-D2 method.⁸ The symmetrization was switched off and the dipolar correction was included. The crystal orbital Hamiltonian population (COHP) was obtained by LOBSTER code.⁹⁻¹² The phononic dispersion curves of RhB was obtained by *phonopy* (2.8.1) with Density Functional Perturbation Theory (DFPT) method.¹³

The lattice parameters of different bulk models were shown in Table S3. The optimized volumes of the *fcc*-Rh and *hcp*-Rh were obtained by fitting the energy-volume data, which was processed by the Equation of state (EOS) program of *VASP*KIT¹⁴ based on Birch-Murnaghan 4th-order EOS.¹⁵ The strain is evaluated by the equation 3:

$$\text{Strain (\%)} = \frac{a - a_0}{a_0} \times 100 \% \quad \text{Eqn. 3}$$

which a_0 and a are the original lattice parameter and strained lattice parameter, respectively.¹⁶ The values of strain for different models were shown in Table S4.

The formation energy of RhX (X = B, C and N) was calculated by the equation 4:

$$\Delta E_f = \frac{E_{\text{total}}(\text{RhX}) - E_{\text{total}}(\text{Rh}) - E_{\text{total}}(\text{X})}{2} \quad \text{Eqn. 4}$$

where $E_{\text{total}}(\text{RhX})$ is the total energy for one formula unit of the RhX, $E_{\text{total}}(\text{Rh})$ and $E_{\text{total}}(\text{X})$ are the energies of pure metal Rh, α -B, graphite and gas N₂ at the ground state, respectively.

The models of *hcp*-Rh (0001) and *fcc*-Rh (111) contain six atom layers, RhB (001) and Pt (111) contain four atom layers, respectively. All the upper half atom layers were

fully relaxed and the remaining were kept frozen during computational process. The 15 Å vacuum layer was selected to avoid interlayer interactions.

The adsorption energy of atomic hydrogen (ΔE_{H^*}) for different site was calculated by the equation 5:

$$\Delta E_{H^*} = E(\text{surface}+H) - E(\text{surface}) - 1/2E(H_2) \quad \text{Eqn. 5}$$

and the ΔE_{H^*} of varying hydrogen coverage (θ_{H^*}) was calculated by the equation 6:

$$\Delta E_{H^*} = E(\text{surface}+nH) - E[\text{surface}+(n-1)H] - 1/2E(H_2) \quad \text{Eqn. 6}$$

which θ_{H^*} is defined as n/N , where n is number of H^* on the surface and N is the number of surface metal atom in the slab models. The adsorption free energy of atomic hydrogen (ΔG_{H^*}) was calculated by the equation 7:

$$\Delta G_{H^*} = \Delta E_{H^*} + \Delta ZPE - T\Delta S \quad \text{Eqn. 7}$$

where ΔZPE and ΔS were the zero-point energy and entropy change of H^* adsorption, respectively. In this work, the ΔZPE and $T\Delta S$ were computed by following the scheme proposed by Norskov *et al.*¹⁷ In particular, ΔS was obtained by equation 8:

$$\Delta S = S(H^*) - 1/2 S(H_2) \approx -1/2S(H_2) \quad \text{Eqn. 8}$$

because vibrational entropy of H^* was negligible. Hence, we can draw the conclusion that the corresponding $T\Delta S$ is -0.205 eV since $TS(H_2)$ is known to be 0.41 eV for H_2 at 298 K and 1 atm. In addition, ΔZPE was obtained by equation 9:

$$\Delta ZPE = ZPE(H^*) - 1/2ZPE(H_2) \quad \text{Eqn. 9}$$

The d -band center (ε_d) can be obtained by equation 10:

$$\varepsilon_d = \frac{\int_{-\infty}^{\infty} n_d(\varepsilon)\varepsilon d\varepsilon}{\int_{-\infty}^{\infty} n_d(\varepsilon)d\varepsilon} \quad \text{Eqn. 10}$$

and d -band width (ε_w) and d -band filling (N_d) can be obtained by equation 11 and 12:

$$\varepsilon_w = \sqrt{\frac{\int_{-\infty}^{\infty} n_d(\varepsilon)(\varepsilon - \varepsilon_d)^2 d\varepsilon}{\int_{-\infty}^{\infty} n_d(\varepsilon)d\varepsilon}} \quad \text{Eqn. 11}$$

$$N_d = \int_{-\infty}^{\varepsilon_F} n_d(\varepsilon)d\varepsilon \quad \text{Eqn. 12}$$

where ε is energy referring to E-Fermi and $n_d(\varepsilon)$ is density of states projected onto d -states.¹⁸ The details of d -band properties were shown in Table S7.

The adsorptions of two hydrogen atoms and hydrogen molecule for RhB (001) were taken as initial state and final state of the Tafel pathway ($H^* + H^* \rightarrow H_2$). The

transition state of reaction was obtained by the climbing image nudged elastic band (CI-NEB)¹⁹ and dimer method²⁰, then confirmed by following vibrational frequency analysis. The activation energies (E_a) were calculated by equation 13:

$$E_a = E_{TS} - E_{ini} \quad \text{Eqn. 13}$$

where E_{TS} and E_{ini} is the energy of transition state and initial state adsorption of hydrogen on the substrate

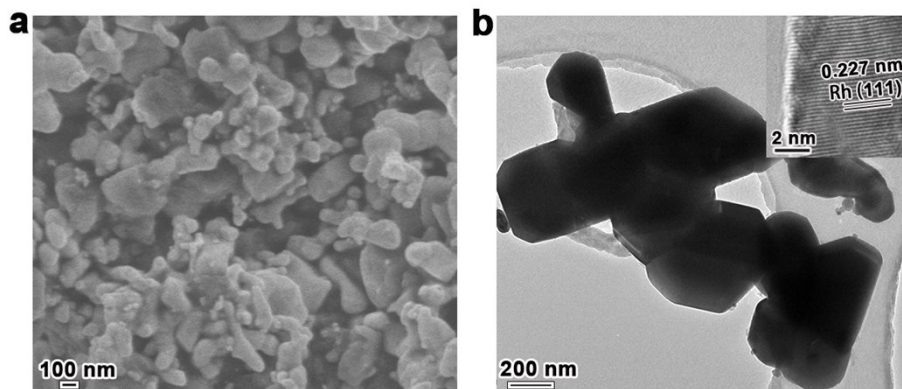


Figure S1 (a) The SEM image and TEM image of Rh particles. The inset image in (b) is the HRTEM of Rh particles. The Rh sample is composed of particles 0.1-1.0 μm in size.

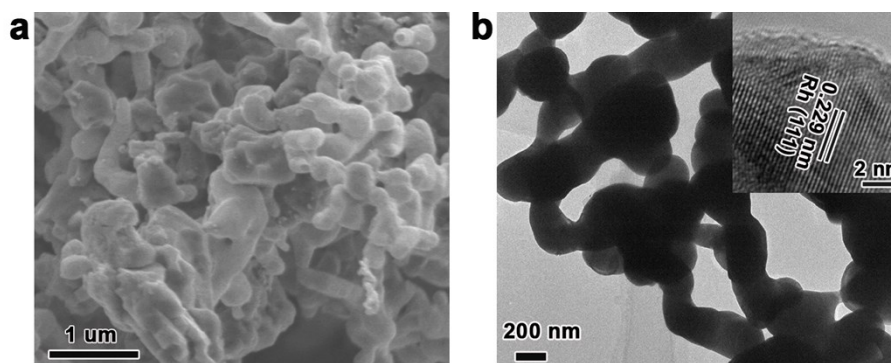


Figure S2 (a) The SEM image and TEM image image of B-Rh particles. The inset image in (a) is the HRTEM of B-Rh particles. The B-Rh sample is composed of particles 0.1-1.0 μm in size.

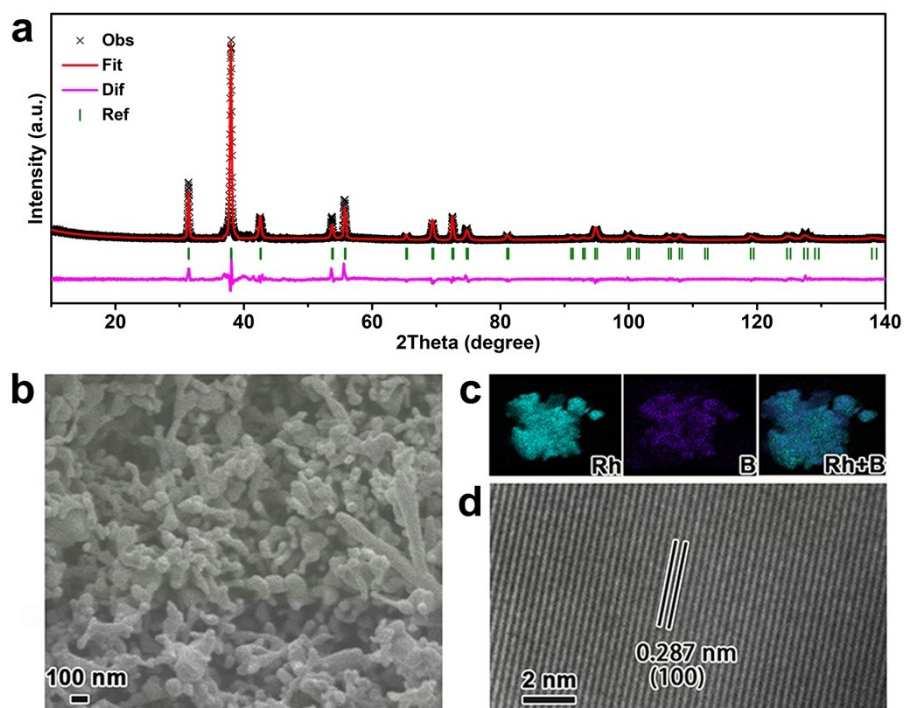


Figure. S3 (a) XRD pattern with a refinement plot of RhB. (b) SEM image of RhB. (c) The EDX elemental mapping images of RhB. (d) TEM image of RhB.

Table S1 The crystallographic information for RhB according to the XRD profile fitting results.

Chemical name	Rhodium Boride
Chemical formula	RhB
Crystal system	Orthorhombic
Space group	P63/mmc
Chemical formula weight (g/mol)	113.72
Cell length a (Å)	3.309(1)
Cell length b (Å)	3.309(1)
Cell length c (Å)	4.224(1)
Cell angle α (°)	90.0
Cell angle β (°)	90.0
Cell angle γ (°)	120.0
Cell volume (Å ³)	40.05
Cell formula units Z	2
Reduced χ^2	3.372
wR _p	0.1683
R _p	0.1227

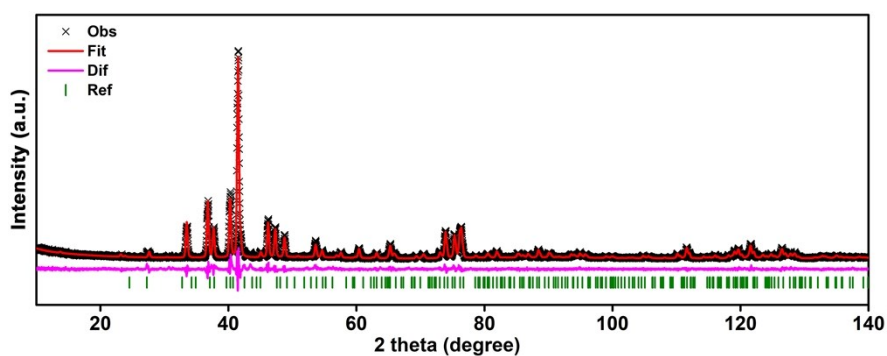


Figure S4 XRD pattern with a refinement plot of Rh₇B₃.

Table S2 The crystallographic information for Rh₇B₃ according to the XRD profile fitting results.

Chemical name	Rhodium Boride
Chemical formula	Rh ₇ B ₃
Crystal system	Orthorhombic
Space group	P63/mmc
Chemical formula weight (g/mol)	752.77
Cell length a (Å)	7.741(1)
Cell length b (Å)	7.741(1)
Cell length c (Å)	4.777(1)
Cell angle α (°)	90.0
Cell angle β (°)	90.0
Cell angle γ (°)	120.0
Cell volume (Å ³)	230.91
Cell formula units Z	2
Reduced χ^2	6.332
wR _p	0.0931
R _p	0.0744

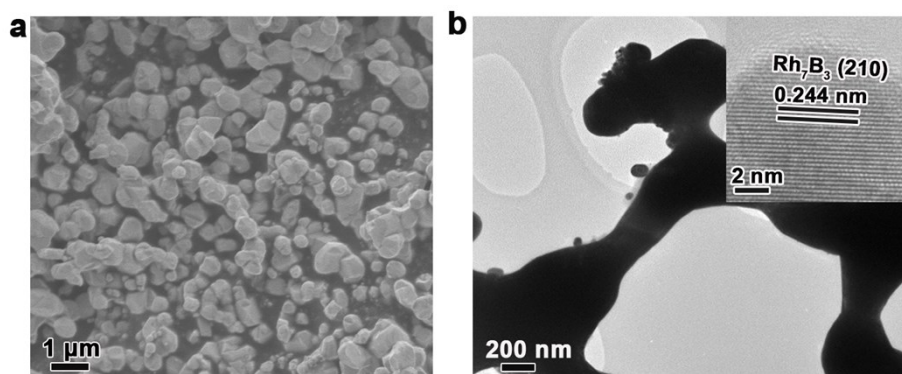


Figure S5 (a) SEM image and (b) TEM image of Rh_7B_3 particles. The inset image in (a) is the HRTEM of Rh_7B_3 particles. The Rh_7B_3 sample is composed of particles 0.1-1.0 μm in size.

Table S3 The lattice parameters of different bulk models.

	a (Å)	b (Å)	c (Å)	Volume (Å ³ per metal atom)
fcc-Rh	3.831	3.831	3.831	14.06
hcp-Rh	2.730	2.730	4.375	14.11
RhB	3.373	3.373	4.148	20.44
RhC	2.952	2.952	5.367	20.25
RhN	3.002	3.002	5.372	20.96
hcp-Rh at 20.44 Å ³	3.082	3.082	4.970	20.44

Table S4 The strain values of different directions for RhB, RhN and RhC compared with *hcp*-Rh at the optimized volume. The negative value represents the compressive strain, and the positive value represents the tensile strain.

	a (%)	b (%)	c (%)
RhB	24	24	-5
RhC	8	8	23
RhN	10	10	23

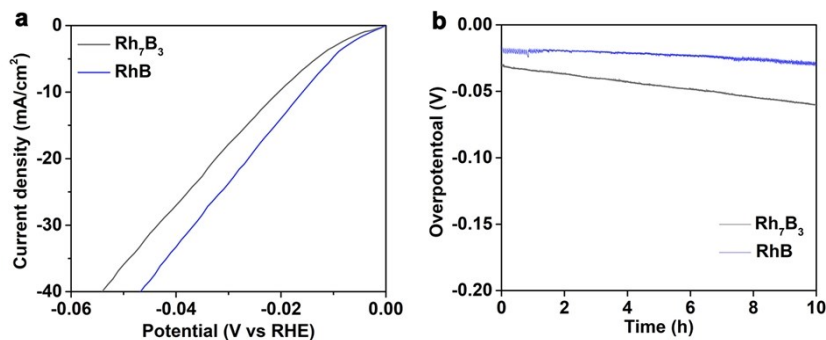


Figure S6 (a) LSV curves and (b) chronopotentiometric curves of Rh_7B_3 and RhB tested in 0.5 M H_2SO_4 electrolyte.

The electrocatalytic activity of Rh_7B_3 for HER was evaluated in acidic solution (Figure S6a). Rh_7B_3 also has good catalytic activity, giving current density of 10 mA/cm^2 at an overpotential of 25 mV. However, the catalytic activity of Rh_7B_3 decreases slowly, and is less stable than that of RhB (Figure S6b).

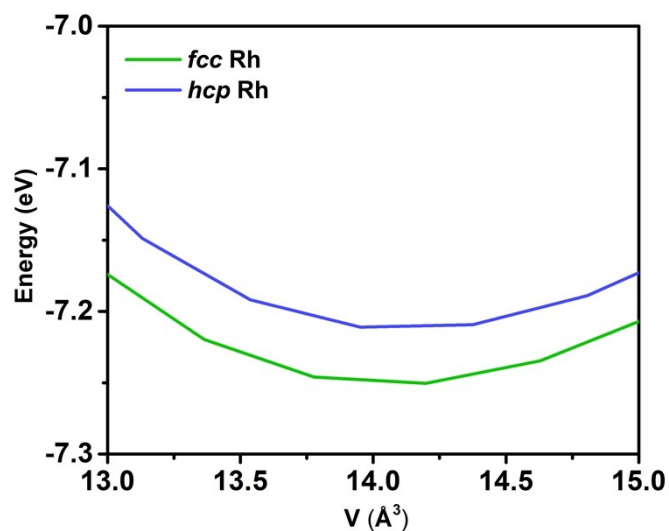


Figure S7 The magnification of equations of state for fcc-Rh and hcp-Rh at the range between 13 and 15 \AA^3 .

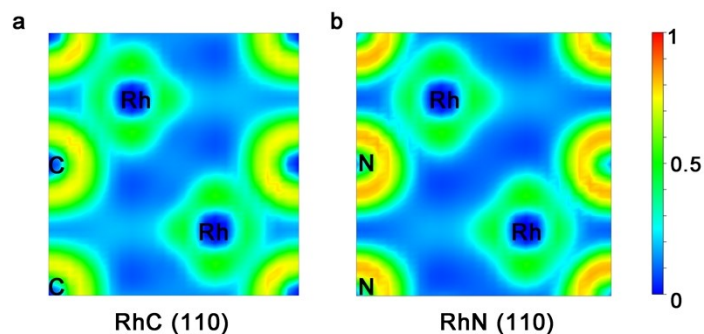


Figure S8 Electron location function (ELF) of (110) crystallographic plane for (a) RhC and (b) RhN. The ELF values between two adjacent carbon atoms for RhC and two adjacent nitrogen atoms for RhN along c axis are ca. 0.1, suggesting there are not bonding interaction between C-C and N-N.

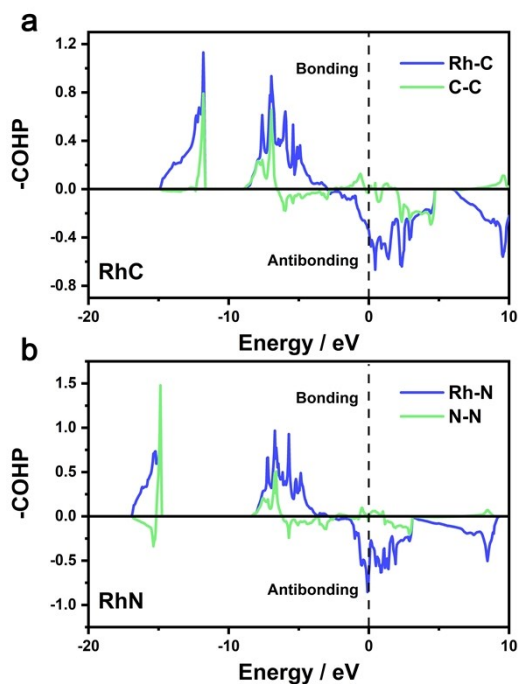


Figure S9 Crystal Orbital Hamilton Populations (COHP) curves of (a) RhC and (b) RhN. The vertical dotted line denotes the position of the Fermi energy.

Table S5 The integrated COHP (-ICOHP) and formation energy of RhB, RhC and RhN.

	-ICOHP of Rh-X (eV)	-ICOHP of X-X (eV)	formation energy (eV /atom)
RhB	2.32	3.76	-0.39
RhC	2.48	0.43	1.10
RhN	1.96	0.14	1.12

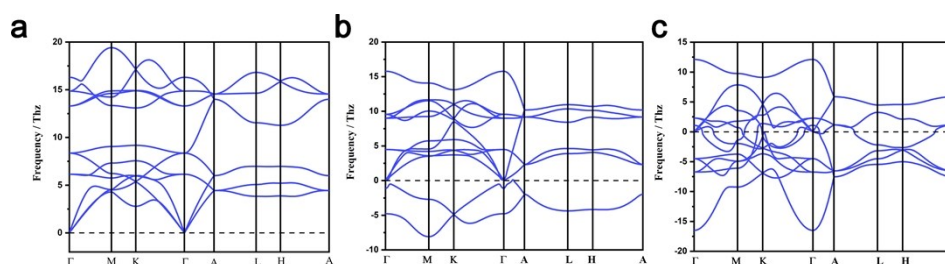


Figure S10 The phononic dispersion curves of (a) RhB, (b) RhC and (c) RhN. As for RhB, there is not imaginary frequency in phonon dispersion of it. But there are imaginary frequencies in phonon dispersion for RhC and RhN, which show that only RhB is dynamically stable.

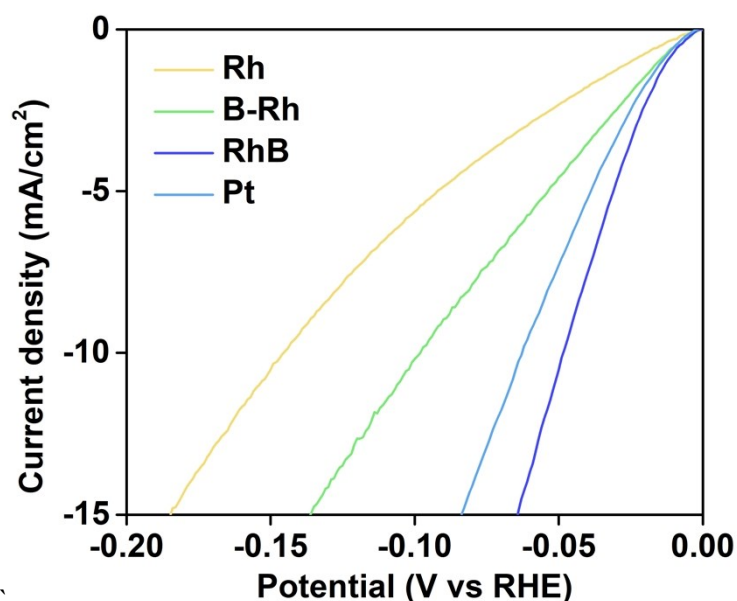


Figure S11 LSV curves of RhB, Rh, B-Rh, and Pt in 1 M KOH solution.

The HER activity of RhB, B-Rh, Rh and Pt were measured in 1 M KOH solution (Figure S11 in SI). RhB requires an overpotential of 40 mV at 10 mA/cm² current density, which were much lower than those of B-Rh (98 mV) and Rh (146 mV), and slightly lower than that of Pt (63 mV). Given that the activity of RhB in alkaline condition is not as good as that in acid solution, we choose acid solution as the electrolyte in this article.

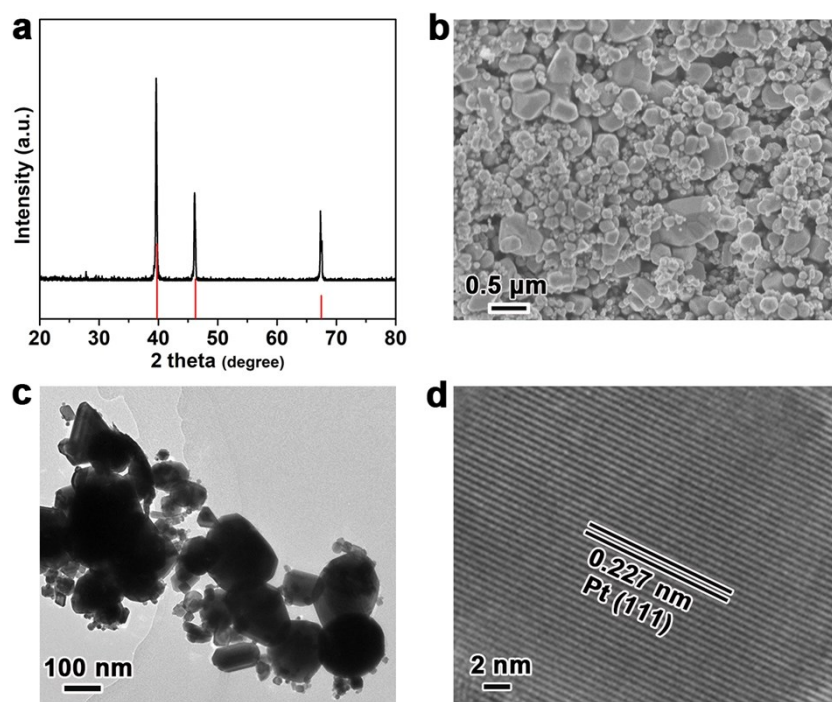


Figure S12 (a) XRD pattern of Pt, using the standard cards of Pt (JCPDS 04-0802) as reference. (b) SEM image, (c) TEM image and (d) HRTEM image of Pt particles. The Pt sample is composed of particles 50-800 nm in size.

Table S6 The comparison of HER performance of RhB with some representative Rh-based electrocatalysts in acidic media.

Catalysts	Loading amount (mg/cm ²)	Overpotential at 10 mA/cm ² (mV)	Scan rate (mV/s)	Stability	Reference
RhB	0.56	15	1	10 h	This work
Rh ₂ S ₃	0.00153	122	2	1000 cycles	21
Rh-MoS ₂	0.309	47	10	22 h	22
Boron-doped RhFe alloy	0.51	25	5	8 h	23
Rh/single-walled carbon nanotubes	0.14	25	5	10000 cycles	24
Rh ₂ P/XC-72	0.153	14	5	16	25
Rh _x P/N, P co-doped carbon	0.21	19	10	20 h	26
RhCu nanotubes	0.15	192	5	12 h	27
Rh/covalent triazine-based framework	0.28	58	20	10000 cycles	28
Rh ₂ P ultrathin nanosheets	0.14	10	5		29
MoS ₂ -confined single atom rhodium	0.50	67	2	1000 cycles	30
Ni _x Rh _{1-x} alloy	0.17	24	10	1000 cycles	31
Rh-Rh ₂ P@C	0.28	24	5	12 h	32
Rh ₂ S ₃ /N-doped carbon hybrids	0.50	21	5	60 h	33
Rh-Au heterostructure	0.28	8.7	5	10000 cycles	34

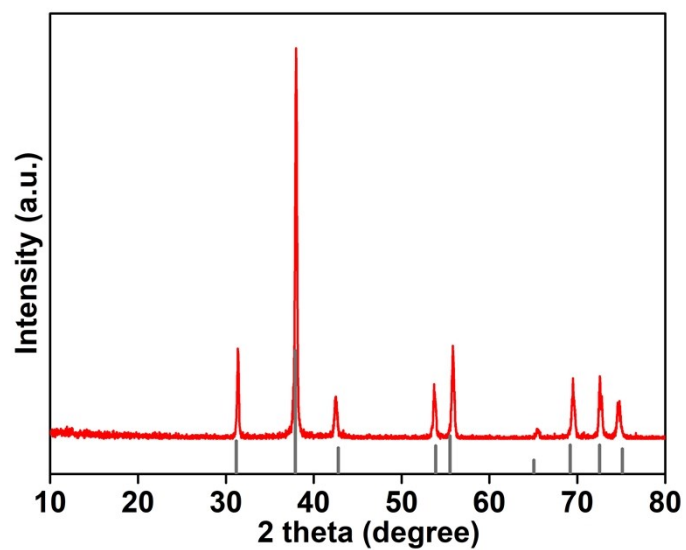


Figure S13 XRD pattern of RhB after 10 h electrocatalysis for HER in 0.5 M H₂SO₄ solution.

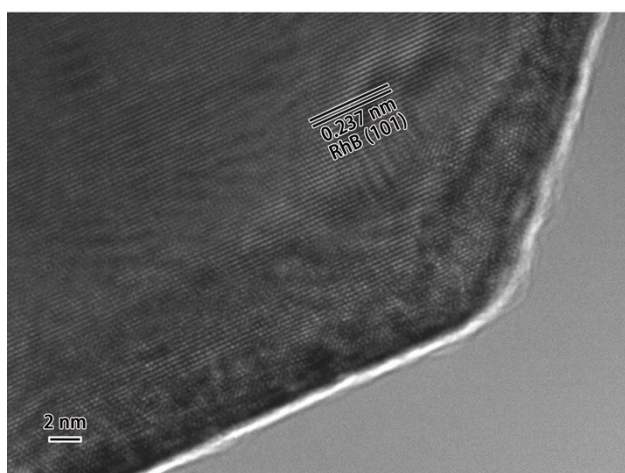


Figure S14 HRTEM image of RhB after 10 h electrocatalysis for HER in 0.5 M H₂SO₄ solution.

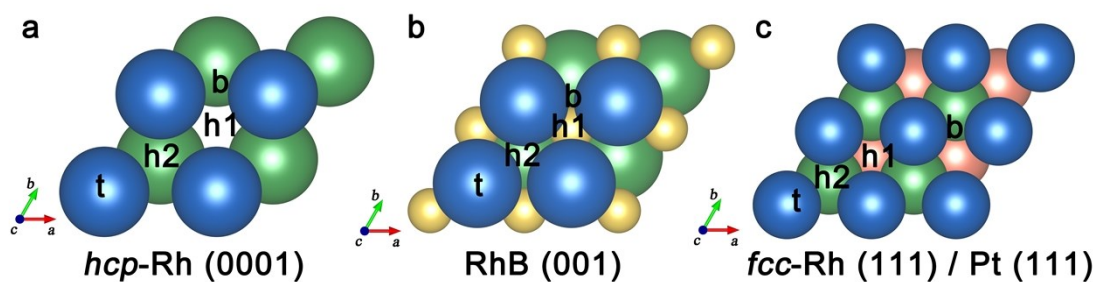


Figure S15 The all adsorption sites for H* on (a) *hcp*-Rh (0001) (b) RhB (001) and (c) *fcc*-Rh / Pt (111). The t, b and h denote the top, bridge and hollow sites, respectively. The blue, green and pink represent the 1st, 2nd and 3rd layer of metal atoms, and the yellow represent B atoms, respectively.

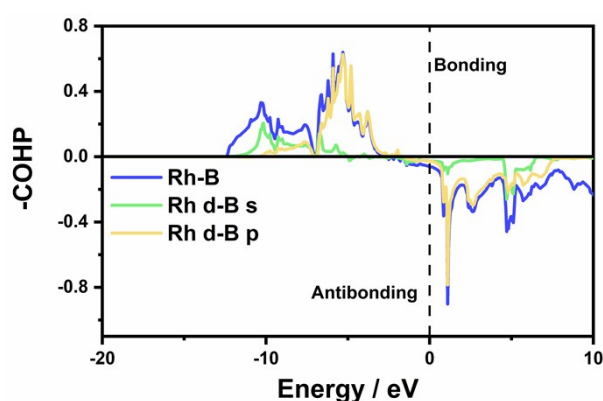


Figure S16 The projected COHP of Rh-B pair in RhB. The vertical dotted line denotes the position of the Fermi energy.

Table S7 The ΔE_{H^*} (eV) at different sites (Figure S15) for different surface. The bold values are ΔE_{H^*} (eV) and ΔG_{H^*} (eV) obtained at 100 % H* coverage on the most stable adsorption sites.

	t	h1	h2	b	ΔE_{H^*} at 100%	ΔG_{H^*} at 100%
<i>fcc</i> -Rh(111)	-0.29	-0.60	-0.58	-0.50	-0.53(h1)	-0.30(h1)
<i>hcp</i> -Rh(0001)	-0.37	-0.65	-0.62	/	-0.59(h1)	-0.36(h1)
RhB(001)	-0.19	-0.25	-0.50	/	-0.35(h1)	-0.18(h1)
Pt(111)	-0.56	-0.54	-0.49	-0.52	-0.36(t)	-0.11(t)

Table S8 The *d*-band center, *d*-band filling and *d*-band width of *hcp*-Rh (0001) and RhB (001).

	<i>d</i> -band center (eV)	<i>d</i> -band filling (per atom)	<i>d</i> -band width (eV)
<i>hcp</i> -Rh (0001)	-1.83	6.67	2.37
RhB (001)	-2.12	7.23	2.70

References

- 1 S. M. Stevens, *Chem. Mater.*, 2016, **29**, 120–140.
- 2 H. Chen, X. Ai, W. Liu, Z. Xie, W. Feng, W. Chen and X. Zou, *Angew. Chem. Int. Ed.*, 2019, **58**, 11409-11413
- 3 J. P. Perdew, K. Burke and M. Ernzerhof, *Phys. Rev. Lett.*, 1996, **77**, 3865-3868.
- 4 P. E. Blöchl, *Phys. Rev. B*, 1994, **50**, 17953-17979.
- 5 G. Kresse and J. Furthmüller, *Comput. Mater. Sci.*, 1996, **6**, 15-50.
- 6 G. Kresse and J. Furthmüller, *Phys. Rev. B*, 1996, **54**, 11169-11186.
- 7 H. J. Monkhorst and J. D. Pack, *Phys. Rev. B*, 1976, **13**, 5188-5192.
- 8 S. Grimme, *J. Comput. Chem.*, 2006, **27**, 1787-1799.
- 9 R. Dronskowski and P. E. Blöchl, *J. Phys. Chem.*, 1993, **97**, 8617-8624.
- 10 V. L. Deringer, A. L. Tchougreff and R. Dronskowski, *J. Phys. Chem. A*, 2011, **115**, 5461-5466.
- 11 S. Maintz, V. L. Deringer, A. L. Tchougreff and R. Dronskowski, *J. Comput. Chem.*, 2013, **34**, 2557-2567.
- 12 S. Maintz, V. L. Deringer, A. L. Tchougreff and R. Dronskowski, *J. Comput. Chem.*, 2016, **37**, 1030-1035.
- 13 A. Togo and I. Tanaka, *Scr. Mater.*, 2015, **108**, 1-5.
- 14 V. Wang, N. Xu, J. Liu, G. Tang and W. Geng, 2019, arXiv:1908.08269.
- 15 F. Birch, *Phys. Rev.*, 1947, **71**, 809.
- 16 P. Strasser, S. Koh, T. Anniyev, J. Greeley, K. More, C. Yu, Z. Liu, S. Kaya, D. Nordlund, H. Ogasawara, M. Toney and A. Nilsson, *Nat. Chem.*, 2010, **2**, 454-460.
- 17 J. K. Nørskov, T. Bligaard, A. Logadottir, J. R. Kitchin, J. G. Chen, S. Pandalov and U. Stimming, *J. Electrochem. Soc.*, 2005, **152**, J23-J26.
- 18 A. Vojvodic, J. K. Nørskov and F. Abild-Pedersen, *Top. Catal.*, 2014, **57**, 25-32.
- 19 G. Henkelman, P. Uberuaga, H. Jónsson, *J. Chem. Phys.*, 2000, **113**, 9901.
- 20 G. Henkelman and H. Jónsson, *J. Chem. Phys.*, 1999, **111**, 7010.
21. D. Yoon, B. Seo, J. Lee, K. S. Nam, B. Kim, S. Park, H. Baik, S. Hoon Joo and K. Lee, *Energy Environ. Sci.*, 2016, **9**, 850-856.

22. Y. Cheng, S. Lu, F. Liao, L. Liu, Y. Li and M. Shao, *Adv. Funct. Mater.*, 2017, **27**, 1700359.
23. L. Zhang, J. Lu, S. Yin, L. Luo, S. Jing, A. Brouzgou, J. Chen, P. K. Shen and P. Tsiakaras, *Appl. Catal. B: Environ.*, 2018, **230**, 58-64.
24. W. Zhang, X. Zhang, L. Chen, J. Dai, Y. Ding, L. Ji, J. Zhao, M. Yan, F. Yang, C.-R. Chang and S. Guo, *ACS Catal.*, 2018, **8**, 8092-8099.
25. F. Yang, Y. Zhao, Y. Du, Y. Chen, G. Cheng, S. Chen and W. Luo, *Adv. Energy Mater.*, 2018, **8**, 1703489.
26. Q. Qin, H. Jang, L. Chen, G. Nam, X. Liu and J. Cho, *Adv. Energy Mater.*, 2018, **8**, 1801478.
27. D. Cao, H. Xu and D. Cheng, *Adv. Energy Mater.*, 2020, **10**, 1903038.
28. M. Siebels, C. Schlüsener, J. Thomas, Y.-X. Xiao, X.-Y. Yang and C. Janiak, *J. Mater. Chem. A*, 2019, **7**, 11934-11943.
29. Y. Zhao, N. Jia, X.-R. Wu, F.-M. Li, P. Chen, P.-J. Jin, S. Yin and Y. Chen, *Appl. Catal. B: Environ.*, 2020, **270**, 118880.
30. X. Meng, C. Ma, L. Jiang, R. Si, X. Meng, Y. Tu, L. Yu, X. Bao and D. Deng, *Angew. Chem. Int. Ed.*, 2020, **59**, 10502-10507.
31. D. Jin, A. Yu, Y. Lee, M. H. Kim and C. Lee, *J. Mater. Chem. A*, 2020, **8**, 8629-8637.
32. L. G. F. Luo, a Y. Xie, J. Xu, W. Cai, K. Qu and Z. Yang, *J. Mater. Chem. A*, 2020, **8**, 7.
33. C. Zhang, H. Liu, Y. Liu, X. Liu, Y. Mi, R. Guo, J. Sun, H. Bao, J. He, Y. Qiu, J. Ren, X. Yang, J. Luo and G. Hu, *Small Methods*, 2020, **4**, 2000208.
34. J. Liu, W. Niu, G. Liu, B. Chen, J. Huang, H. Cheng, D. Hu, J. Wang, Q. Liu, J. Ge, P. Yin, F. Meng, Q. Zhang, L. Gu, Q. Lu and H. Zhang, *J. Am. Chem. Soc.*, 2021, **143**, 4387-4396.